Sánchez-González, A. & Yellowhair, J. (2020). Reflections between heliostats: Model to detect alignment errors. *Solar Energy, 201*, 373–386.

DOI: 10.1016/j.solener.2020.03.005

Reflections between heliostats: model to detect alignment errors

Alberto Sánchez-González[a,*], Julius Yellowhair[b]

[a]*Energy Systems Engineering Group (ISE), Department of Thermal and Fluid Engineering, Universidad Carlos III de Madrid, Av. Universidad, 30, 28911, Leganés, Madrid, Spain*

[b]*Concentrating Solar Technologies Department, Sandia National Laboratories, P.O. Box 5800, MS-1127, Albuquerque, NM 87185-1127, USA*

Abstract

Keywords: Solar power tower, Heliostat optical quality, Facet canting & focusing, Pinhole camera model, Alhazen's problem

1. Introduction

In Solar Power Tower (SPT) plants, thousands of heliostats –tracking mirrors– concentrate sunlight into a receiver on the top of a tower, to eventually produce electricity from the highly heated working fluid. The reflecting surface of a heliostat, typical commercial size around 120 m^2, consists of a subset of slightly curved mirrors –facets– that are aligned to concentrate direct solar radiation as much as possible; i.e. reduce spot size and spillage losses in the receiver.

Heliostat alignment involves two actions: focusing and canting. Mirror focusing consists in slightly curving the facet surface into a concave shape. Heliostat canting consists in tilting each facet to point at a single aimpoint. Heliostat alignment leads to reduced spot size and spillage losses in the receiver, as a result annual power intercepted by the receiver is maximized (Jones, 1996).

Existing methods for alignment of mirror facets can be grouped into three categories (Yellowhair and Ho, 2010; Ren et al., 2014): on-sun, mechanical,

*Corresponding author

Email address: asgonzal@ing.uc3m.es (Alberto Sánchez-González)

and optical. In on-sun alignment, single facets –being the rest covered– are qualitatively adjusted by visual inspection of the beam shape on the target. This technique is imprecise and time consuming. Mechanical alignment can be performed by means of gauge blocks or inclinometers placed on the facets, while the heliostat is in horizontal position. This procedure is very time consuming and just canting can be corrected.

OPTICAL TECHNIQUES
Photogrammetry (Röger et al., 2008)
Deflectometry or fringe reflection, AIMFAST-SOFAST: detection of slope error (Andraka et al., 2009)
Laser beams
Beam shape optimization (Sánchez-González et al., 2017)
Camera look-back (Jones et al., 1994)
Target reflection (H-FACET) (Sproul et al., 2011)

To overcome the limitations of existing alignment methods, a novel technique is described in the present paper. This methodology combines aerial vision with theoretical imaging to detect heliostat alignment errors while heliostats are under operation in the plant (Yellowhair, 2019) (patent?).

The main goal of the present work is to describe in detail the theoretical background and validate the model employed by this technique.

The manuscript is structured as follows. Firstly, an overview on the alignment tool is presented. Then, the optical model is detailed describing the underlying concepts: transformation of coordinate systems, pinhole camera model and determination of reflection points. Subsequently, the optical model is validated against actual photos of heliostats reflecting others. A sensitivity analysis in terms of pixel shift detection is then presented. And, finally, conclusions are offered.

2. Alignment tool

The basis of the model presented in this work is similar to that of H-FACET. A camera pointing to the object heliostat reflects a neighbour target. Deviations between actual –from the camera– and theoretical –from an optical model– images allows to detect alignment errors in the object heliostat.

In H-FACET the camera was placed atop the tower. Now, the camera is mounted on an Unnamed Aerial System (UAS). This way, heliostats to assess

can be under operation at the same time. The back of a neighbor heliostat is used as the target and its facet edges are taken as the feature of reference. A brief comparison between H-FACET and the new tool is summarized in Table 1.

Table 1: Comparison between the new tool and H-FACET.

	H-FACET	**New tool**
Heliostat mode	Out of operation	In operation (no interruption)
Camera position	Fixed (top of the tower)	Movable (mounted on UAS)
Target	Movable target	Neighbor heliostat
Feature in target	Cross (facet center)	Facet edges
Assessment goal	Canting	Full alignment (canting & focusing)

Fig. 1 depicts the principle of the proposed alignment tool. While heliostats are under operation, a camera mounted on an UAS points at the object heliostat to see in reflection the back of the target (neighbor) heliostat. Images taken from the camera and showing the target heliostat in reflection are compared to the theoretical ones, according to the optical model presented in the following. Finally, it is gathered the alignment deviations –both for facet canting and focusing– in the object heliostat.

While the heliostat is under operation, it is oriented so that its normal, $\mathbf{n_h}$, is in the bisector between unit vectors $\mathbf{s}$, pointing to the Sun, and $\mathbf{a}$, directed to aimpoint A (i.e. $\mathbf{a} = \overline{HA} \big/ \left|\overline{HA}\right|$, being H the position of the heliostat center). Mathematically this is expressed by Snell reflection law, Eq. 1. Along the manuscript and as used before, bold lowercase and normal uppercase letters respectively represent unit vectors and point position vector.

$$\mathbf{n_h} = \frac{\mathbf{s} + \mathbf{a}}{|\mathbf{s} + \mathbf{a}|} \tag{1}$$

In order to see the target heliostat, centered in T, the camera C must be located along the line defined by unit vector $\mathbf{c}$. Being $\mathbf{t}$ the unit vector

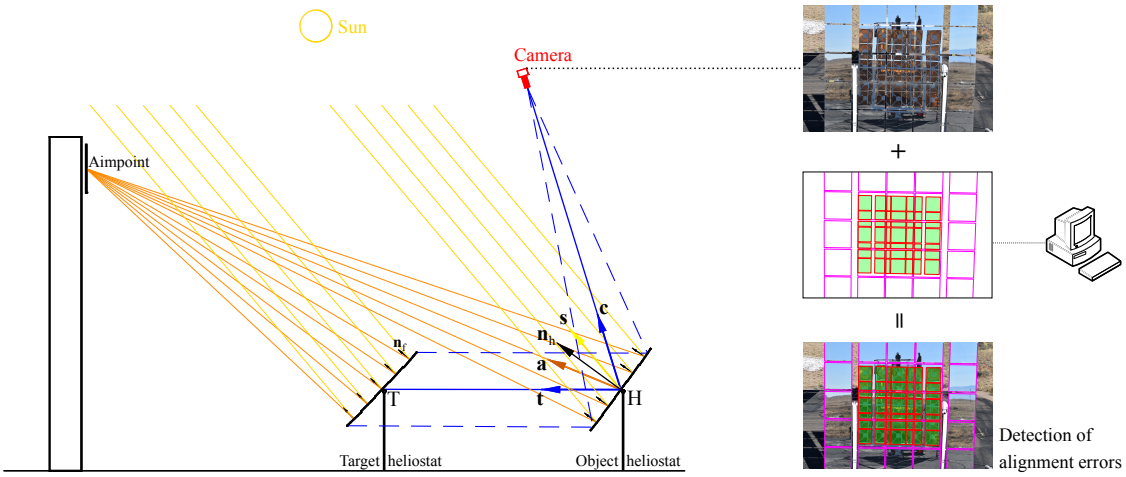

Figure 1: Alignment tool.

from H to T, reflection law again applies, turning into Eq. 2. The specific heliostat-to-camera distance (i.e. $\left|\overline{HA}\right|$) depends on the zoom focal length and region of interest to be captured.

$$\mathbf{c} = 2\,(\mathbf{n_h} \cdot \mathbf{t})\,\mathbf{n_h} - \mathbf{t} \tag{2}$$

3. Optical model

This section puts forward the background supporting the optical model to accurately compute the theoretical images. At the beginning, the reference systems of coordinates and transformations between them are presented. Then, the underlying pinhole camera model and the determination of reflection points are described. Finally, they are detailed the steps contained in the computational code in order to generate the theoretical images.

3.1. Coordinate systems and transformations

Five main orthogonal systems of coordinates are defined, namely: global (sg), heliostat (sh), target (st), facet (sf) and camera (sc) with origins in G, H, T, F and C, respectively. The global system of coordinates has origin in G tower base. Positive X_{sg} and Y_{sg} axes correspondingly point to East and North. As right-handed system, Z_{sg} aims at the Zenith.

Fig. 2 depicts those 3D coordinate systems. Unit vectors in the positive directions of X, Y and Z axes are respectively symbolized by $\mathbf{u}$, $\mathbf{v}$ and $\mathbf{w}$.

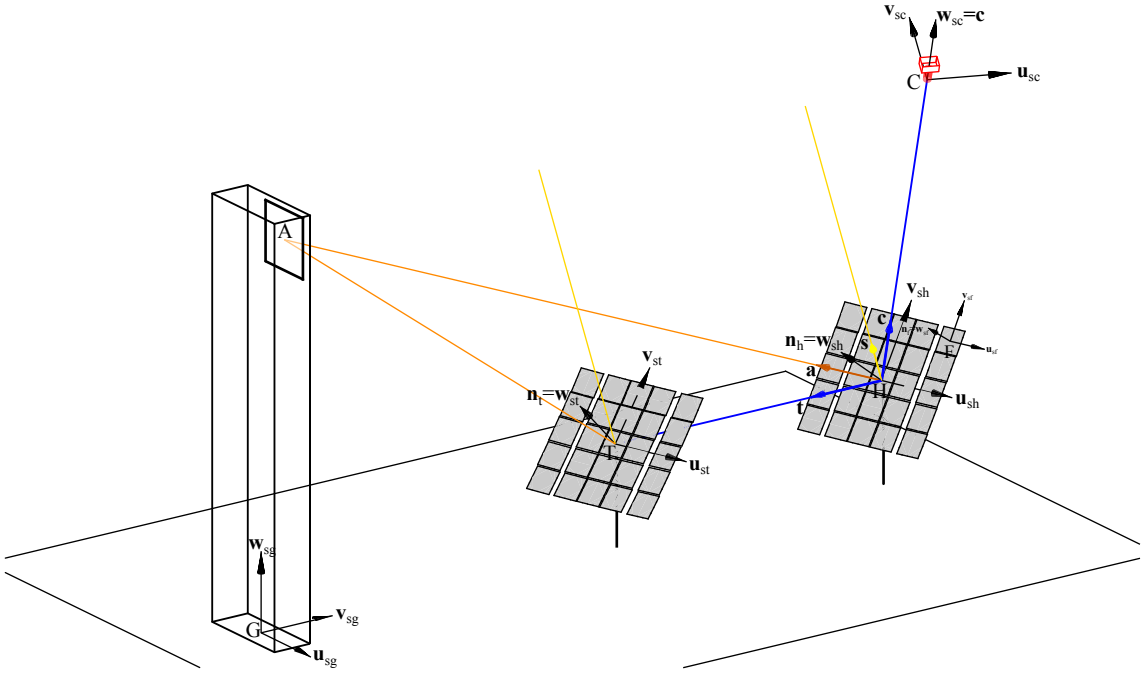

Figure 2: Systems of coordinates.

In the heliostat systems of coordinates, either object (sh) or target (st), Z_{sh} is collinear with heliostat normal $\mathbf{n_h}$. For azimuth-elevation tracking heliostats, X_{sh} remains horizontal like the axis of elevation.

For each facet, an specific coordinate system with origin in its center, F, is defined. Z_{sf} is again collinear with the facet normal $\mathbf{n_f}$, while X_{sf} and Y_{sf} are respectively parallel to top-bottom and lateral edges of the facet, in conventional rectangular/square facets.

Finally, the camera system of coordinates has Z_{sc} axis collinear with vector $\mathbf{c}$, obtained from Eq. 2. $X_{sc}Y_{sc}$ plane is parallel to the image plane of the camera.

Geometric transformations between systems of coordinates are handled by the optical model, as described in the following. Given the x,y,z coordinates of a point/facet/surface in a system 'i' (si), the corresponding coordinates in another system 'ii' (sii) result from a geometric rotation and translation, as

mathematically expressed by the following Equation.

$$\begin{bmatrix} x \\ y \\ z \end{bmatrix}_{sii} = \mathbf{ROT_{i2ii}} \cdot \begin{bmatrix} x \\ y \\ z \end{bmatrix}_{si} + \mathbf{transl_{i2ii}} \tag{3}$$

Having origins in points I and II, the translation vector is straightforward (Eq. 4). The rotation matrix depends on the relative orientation of both systems. Such matrix is arranged in Eq. 5, by means of relative azimuth, α, and elevation, ϵ, angles between both systems.

$$\mathbf{transl_{i2ii}} = \begin{bmatrix} I_x - II_x \\ I_y - II_y \\ I_z - II_z \end{bmatrix}_{sii} \tag{4}$$

$$\mathbf{ROT_{i2ii}} = \begin{bmatrix} \cos\alpha & 0 & \sin\alpha \\ \sin\alpha \cdot \sin\varepsilon & \cos\varepsilon & -\cos\alpha \cdot \sin\varepsilon \\ -\sin\alpha \cdot \sin\varepsilon & \sin\varepsilon & \cos\alpha \cdot \cos\varepsilon \end{bmatrix} \tag{5}$$

3.2. Reflection points and pinhole camera

The success of the model relies on an accurate reproduction of the optics taking place. On one hand, as the actual image from the camera is compared with that obtained from the model, it is key an accurate model to emulate camera optics. On the other hand, the reference features to determine alignment errors are the facet edges of the target heliostat seen in reflection in the object heliostat. Therefore, a precise determination of the edges in reflection is required.

For each facet in the target heliostat, its edge is discretized into points, as shown in Fig. 3 for the central facet. The determination of the reflection points in the object heliostat is a classical geometric problem. Naming Q to a point in the facet boundary of the target heliostat, and being the viewpoint –camera– in C, the goal is to find out Q_{ref}, point Q reflected any mirror of the object heliostat. Again reflection law applies, so that in Q_{ref} incident and reflected angles are the same. This problem, which is fairly simple whether the mirror facet surface were flat, is somehow challenging for a real curved facets.

Because of facet focusing, each facet mirror has a spherical –sometimes referred to as paraboloid– curvature. To concentrate the reflected beam in the receiver as much as possible, the focal length of the facet must be equal to

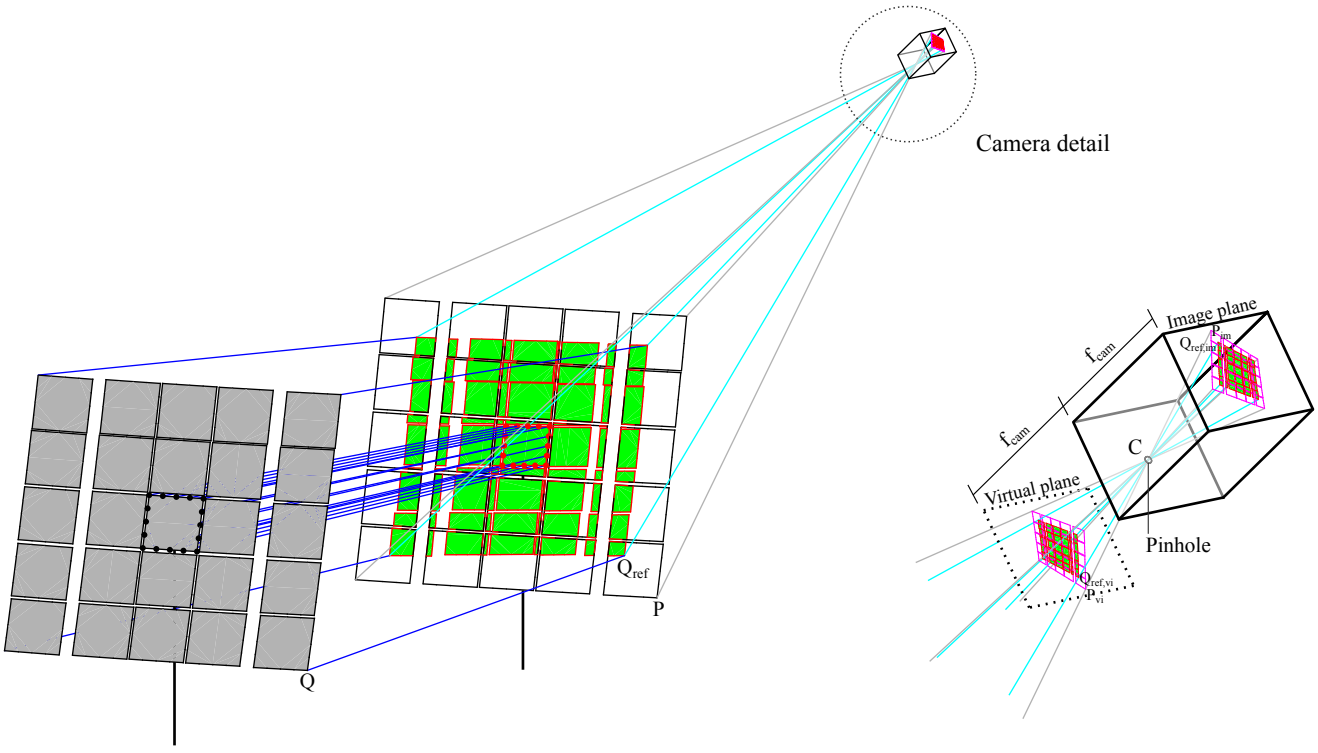

Figure 3: Reflection points.

the facet-to-aimpoint distance. As a consequence, the ideal curvature radius of the spherical mirror is twice such focal length. Thus, the reflected point has to be found in the spherical surface having that curvature.

The reflection point in concave –and convex– spherical mirrors is known as Alhazen's problem (SMITH, 2008). Glaeser (1999) described the way to find the solution point, which lies in the plane containing: the original point, Q, the viewpoint, C, and the center of the sphere, O. Therefore converted into a 2D problem, the solution Q_{ref} is in the tangent point between the circumference (arc) and the ellipse with foci in Q and C. Barone et al. (2018) put into mathematical formulation such geometric solution to Alazen's problem. An adapted version of their *world2cam.m* Matlab code (Neri et al., 2018) has been taken in the present work.

Regarding the camera optics, the classical pinhole –or perspective projection– model (Hartley and Zisserman, 2003) has been adopted herein. This model assumes that all the rays pass through a single point (pinhole), named opti-

cal (or camera) center, C. The line passing through C and any point in the 3D space creates a projection line. At the camera focal length, f_{cam}, from C is the image plane where the 2D image is formed, by the intersection of all the projections lines. The image plane is equivalent to the CCD sensor. For a non-reversed image, a virtual plane located at f_{cam} in front of the pinhole can be considered. These mapping relationships are shown in the camera detail of Fig. 3.

Despite of not considering lenses and aperture size, the pinhole model accurately predicts the behavior of a high quality focused camera. Radial and tangential distortions caused by the lens can be included by obtaining the distortion coefficients by means of camera calibration (Mathworks, 2019).

3.3. Methodology

All the concepts and models mentioned before are put together into a Matlab® script from which theoretical images are generated. This subsection explains the steps followed in order to reach that output.

COMMENT on Fig. 4

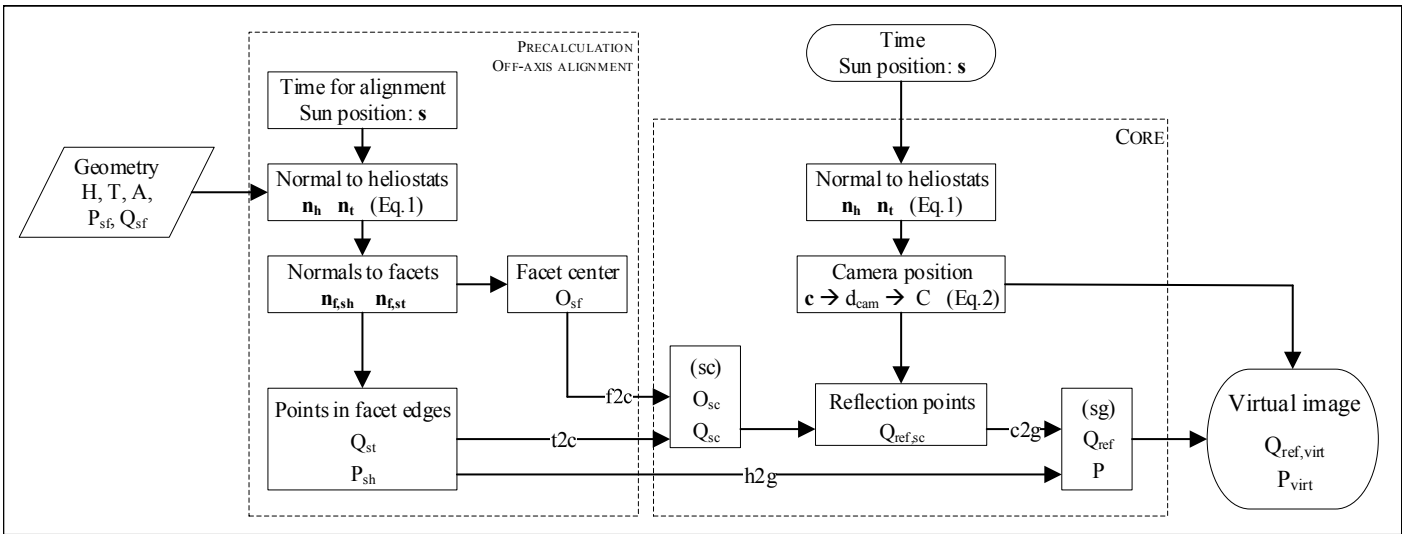

Figure 4: Flowchart of the optical model.

4. Validation

Once the optical model was set, the next step was its validation. Experiments were carried out at the NSTTF heliostat field, operated by SNL. Two heliostats acceptably aligned were used, taking as target heliostat another one in front of each of them. Orientation of the heliostats was set so as to emulate realistic tracking scenarios during heliostat field operation. However, to avoid continuous movement of the camera, heliostats' orientation was kept fixed during the experimental campaign.

For a proper control of the viewpoint, i.e. camera, position, a scissor lift was utilized. Fig. 5 shows one of the experimental setup scenarios with target and object heliostats respectively in left and right sides of the Figure. On a scissor lift, left of target heliostat, images with different focal lengths were captured with a high quality Nikon D3300 camera.

Figure 5: Set-up during experimental campaign.

Experimental images from the camera have been confronted against the simulated images to demonstrate the goodness of the model. In the following, they are shown several superpositions of simulated images over actual photos. Regarding the model output, facet edges of the object heliostat are represented by magenta lines throughout this manuscript. Similarly, the reflected facet edges of the target heliostat are marked in red and the enclosed faces are colored in green.

From the same C viewpoint aimed to heliostat 6E9, both Figures 6 and 7 overlay the theoretical image on the actual images respectively for focal lengths of 18 and 55 mm.

COMMENT ON THE FIGURES

For heliostat 12E14, from a more distant camera position (66.5 m), Fig. 8 shows the comparison when having 300 mm of camera focal length.

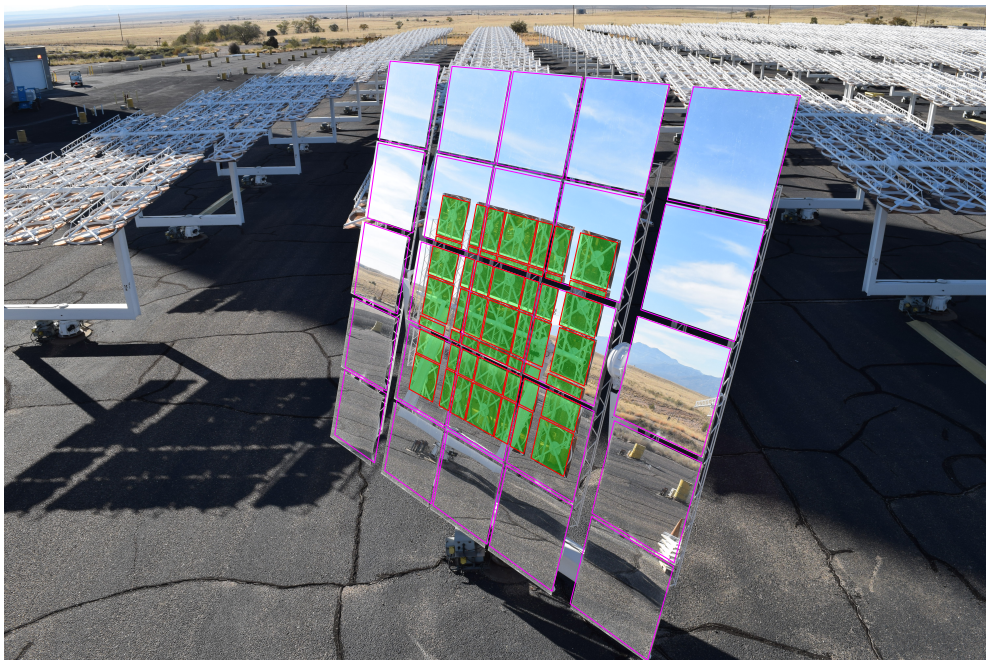

Figure 6: Heliostat 6E9 reflecting 5E9 ($f_{cam} = 18mm$).

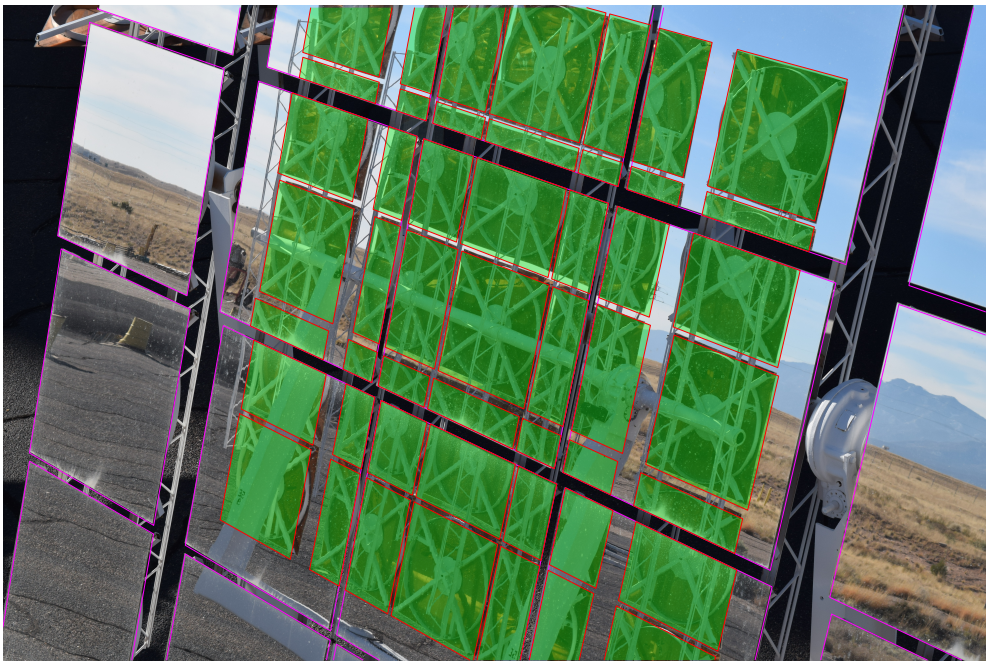

Figure 7: Heliostat 6E9 reflecting 5E9 ($f_{cam} = 55mm$).

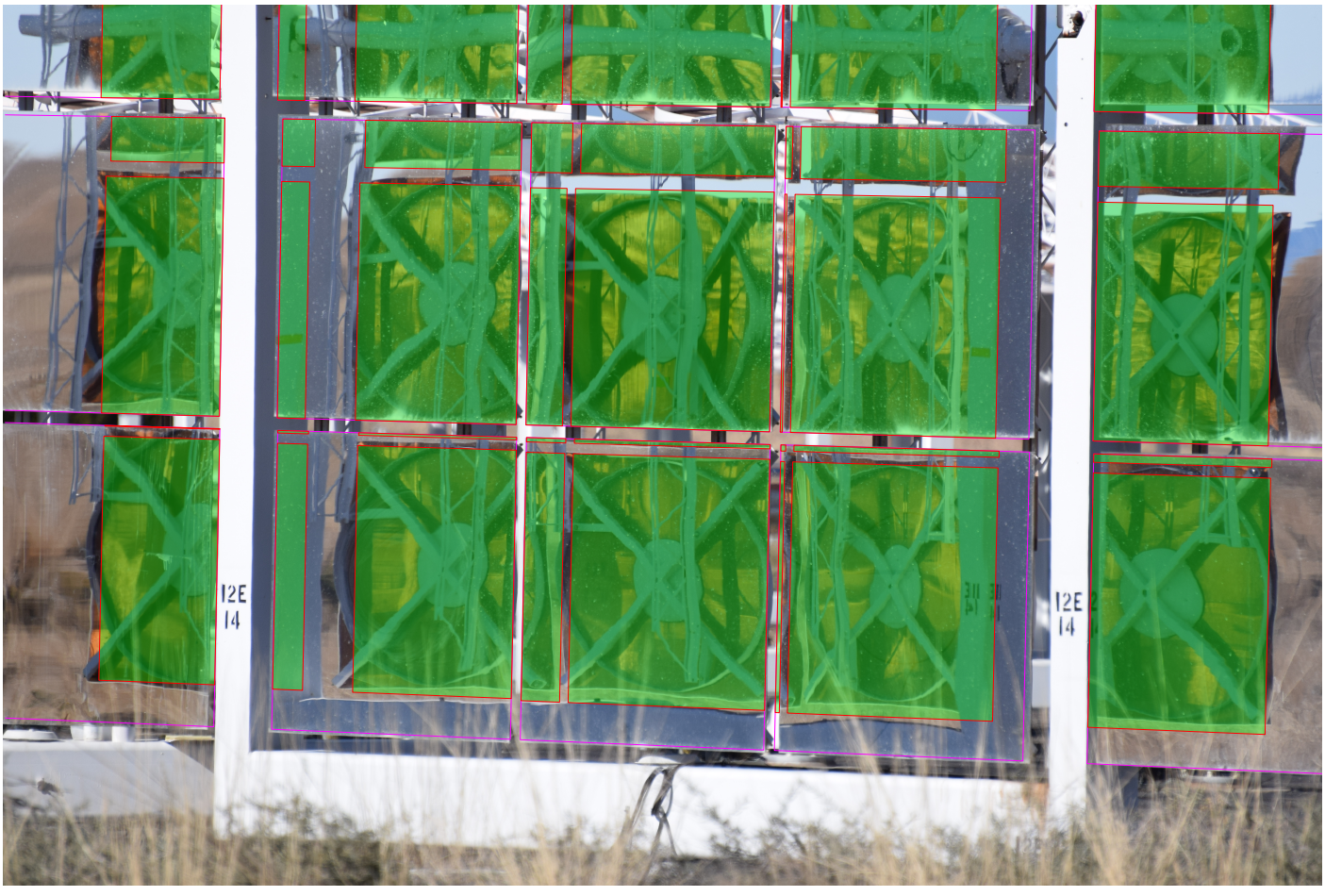

Figure 8: Heliostat 12E14 reflecting 11E14 ($f_{cam} = 300mm$).

5. Sensitivity analysis

In a second round of experimental tests, it was assessed the sensitivity of the optical model, and the alignment tool in general. Heliostat 12E14 was taken as object, seeing target 11E14 in reflection. Photos were taken before and after specific adjustment in selected facets. Specifically, 1 mrad angular movements were performed in the bottom left (only around the vertical axis) and bottom center (around both axes) facets.

The resolution of the employed Nikkon D3300 camera is 6000 x 4000 pixels. Its CCD sensor size is 23.5 x 15.6 mm, then resulting 255 pixels/mm. These figures are important to the optical model in order to predict the pixel shift.

Fig. 9 shows captions of the bottom center facet before (a) and after (b) a 1 mrad angular movement around both axes. From image treatment, the resulting pixel shifts horizontally and vertically are correspondingly -30 (to the left) and -29 (downwards) pixels.

On the other hand, ideally canted and adjusted facet scenarios were simulated with the optical model. Both cases are superimposed in Fig. 10, using blue color to represented the adjusted-second case. As a result, the pixel shift was -36 in horizontal and -27 in vertical.

Results for both the bottom left and bottom center facets are summarized in Table 2.

Table 2: Pixel shift comparison: camera image vs. model.

	Facet	Bottom left		Bottom center	
		x	y	x	y
Angular mov. [mrad]		1	0	1	1
Pixel shift	Camera	-32	1	-30	-29
	Model	-35	1	-36	-27

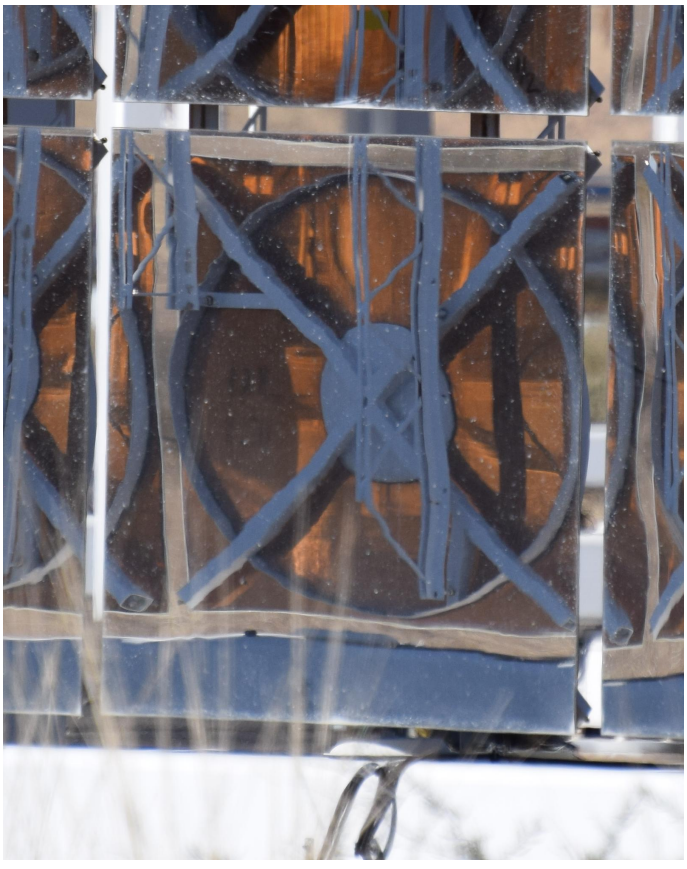

(a) Before adjustment.

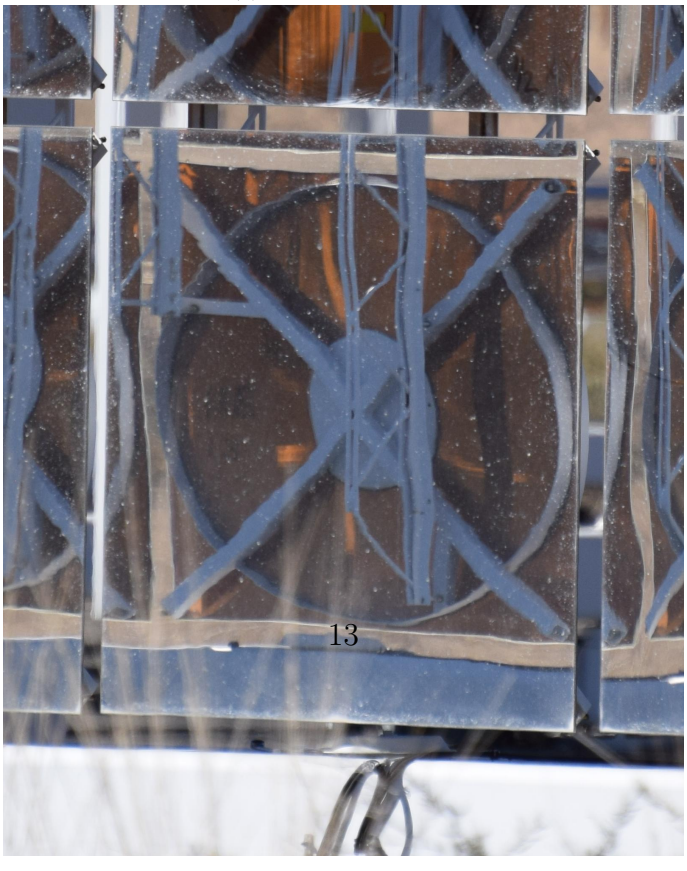

(b) After adjustment.

Figure 9: Images of bottom central facet (heliostat 12E14, $f_{cam} = 300mm$).

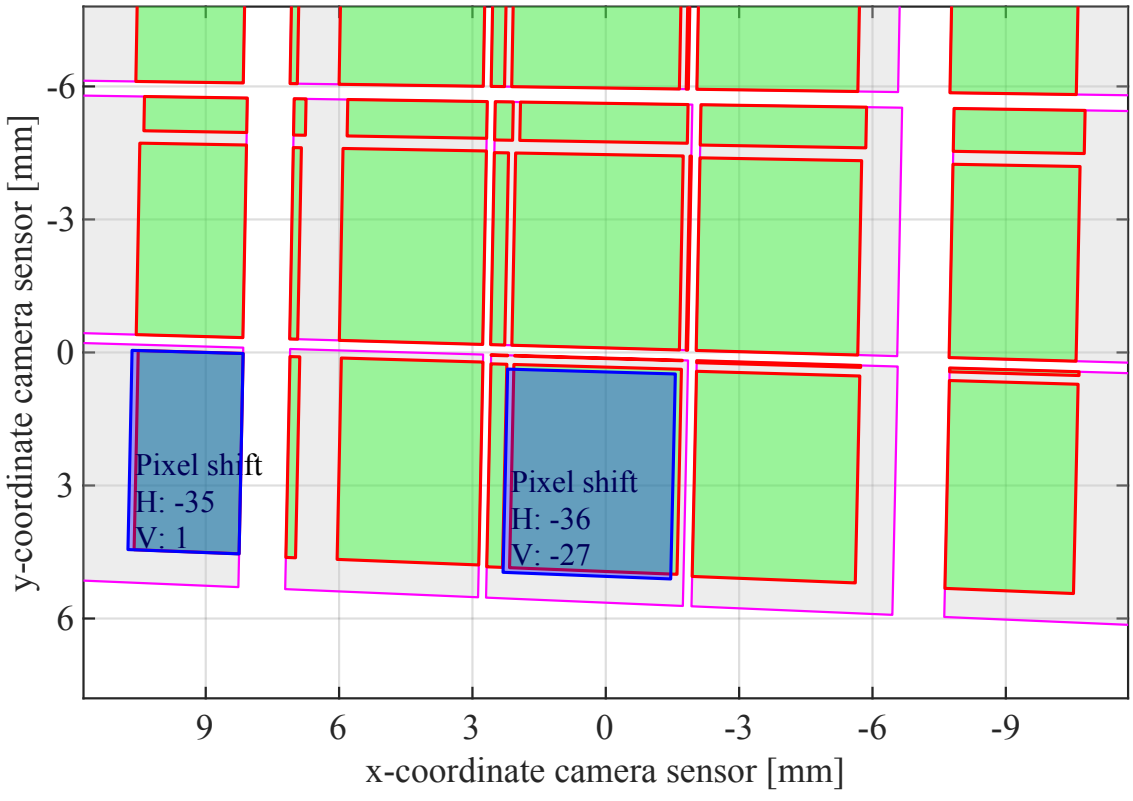

Figure 10: Pixel shifts predicted by the model (heliostat 12E14).

6. Conclusions

Acknowledgments

A. Sánchez-González is indebted to Universidad Carlos III de Madrid for the mobility grant that funded the stay at Sandia National Laboratories during autumn 2018. The authors acknowledge the help provided during the experimental phase by SNL staff: Roger Buck, Joshua Christian, Rio Hatton, Jesus Ortega, Benson Tso, Rip Winckel, David Novick and Daniel Small.

Nomenclature

A	Aimpoint position
a	Aimpoint unit vector
C	Camera position
c	Camera unit vector
f_{cam}	Camera focal length
H	Heliostat (object) position
n	Normal unit vector
O	Center of spherical facet
P	Facet edge point in object heliostat
Q	Facet edge point in target heliostat
ROT	Rotation matrix
s	Sun unit vector
T	Target heliostat position
t	Target unit vector
transl	Translation vector
u,**v**,**w**	Unit vectors in X,Y,Z directions
X,Y,Z	Cartesian coordinate axes
x,y,z	Coordinates in X,Y,Z directions [m]

Greek symbols

α	Azimuth angle [rad]
ϵ	Elevation angle [rad]

Subscripts

f	Facet
h	Heliostat
ref	Reflected
sc	Camera system of coordinates
sf	Facet system of coordinates
sg	Global system of coordinates
sh	Heliostat system of coordinates

Acronyms

NSTTF	National Solar Thermal Test Facility
UAS	Unmanned Aerial System
SNL	Sandia National Laboratories
SPT	Solar Power Tower

References

Andraka, C. E., Sadlon, S., Myer, B., Trapeznikov, K., Liebner, C., 2009. SOFAST: sandia optical fringe analysis slope tool for mirror characterization. Proceedings of Solar Paces, 15–18.

Barone, S., Carulli, M., Neri, P., Paoli, A., Razionale, A., jan 2018. An Omnidirectional Vision Sensor Based on a Spherical Mirror Catadioptric System. Sensors 18 (2), 408.
URL http://www.mdpi.com/1424-8220/18/2/408

Glaeser, G., 1999. Reflections on spheres and cylinders of revolution. Journal for Geometry and Graphics 3 (2), 121–139.
URL https://www.scopus.com/inward/record.uri?eid=2-s2.0-77953252005{\&}partnerID=40{\&}md5=4b317b476f9a8518ae1be85a6c6cfa15

Hartley, R., Zisserman, A., 2003. Multiple view geometry in computer vision. Cambridge university press.

Jones, S. A., 1996. Annual performance prediction for off-axis aligned Lugo heliostats at Solar Two. In: American Society of Mechanical Engineers international solar energy conference. Sandia National Laboratories, SAND-96-0212C, San Antonio, TX (United States).

Jones, S. A., Edgar, R. M., Houser, R. M., 1994. Recent results on the optical performance of solar two heliostats. In: American Society of Mechanical Engineers international solar energy conference. Sandia National Laboratories, SAND-94-2776C, Lahaina, HI (United States).
URL http://www.osti.gov/scitech/biblio/10106656

Mathworks, 2019. What Is Camera Calibration?
URL https://es.mathworks.com/help/vision/ug/camera-calibration.html

Neri, P., Barone, S., Paoli, A., Razionale, A., 2018. Spherical mirror forward and backward projection.
URL https://es.mathworks.com/matlabcentral/fileexchange/65891-spherical-mirror-forward-and-backward-projection

Ren, L., Wei, X., Lu, Z., Yu, W., Xu, W., Shen, Z., 2014. A review of available methods for the alignment of mirror facets of solar concentrator in solar thermal power system. Renewable and Sustainable Energy Reviews 32, 76–83.
URL http://www.sciencedirect.com/science/article/pii/S1364032113008204http://www.sciencedirect.com/science/article/pii/S1364032113008204/pdfft?md5=521c4c1996ac2ee73714b9481cf40a17{\&}pid=1-s2.0-S1364032113008204-main.pdf

Röger, M., Prahl, C., Ulmer, S., 2008. Fast determination of heliostat shape and orientation by edge detection and photogrammetry. In: Proc. 14th CSP SolarPACES Symposium. pp. 4–7.

Sánchez-González, A., Caliot, C., Ferriere, A., Santana, D., 2017. Determination of heliostat canting errors via deterministic optimization. Solar Energy 150, 136–146.
URL http://www.sciencedirect.com/science/article/pii/S0038092X17303328

SMITH, A. M., sep 2008. ALHACEN'S APPROACH TO "ALHAZEN'S PROBLEM". Arabic Sciences and Philosophy 18 (2), 143–163.
URL https://www.cambridge.org/core/product/identifier/S0957423908000520/type/journal{_}article

Sproul, E., Chavez, K., Yellowhair, J., 2011. The Development of the Heliostat Focusing and Canting Enhancement Technique: An Optical Heliostat Alignment Tool for the National Solar Thermal Test Facility. In: ASME 2011 5th International Conference on Energy Sustainability, Parts A, B, and C. ASME, pp. 611–619.
URL http://proceedings.asmedigitalcollection.asme.org/proceeding.aspx?articleid=1636540

Yellowhair, J., 2019. Development of a UAS-Driven Universal Field Assessment, Correction, Enhancement Tool Adopting Non-Intrusive Optics.
URL https://www.energy.gov/eere/solar/downloads/seto-csp-program-summit-2019

Yellowhair, J., Ho, C. K., 2010. Heliostat Canting and Focusing Methods: An Overview and Comparison. In: ASME 2010 4th International Conference on Energy Sustainability, Volume 2. ASME, pp. 609–615.
URL http://proceedings.asmedigitalcollection.asme.org/proceeding.aspx?articleid=1607627